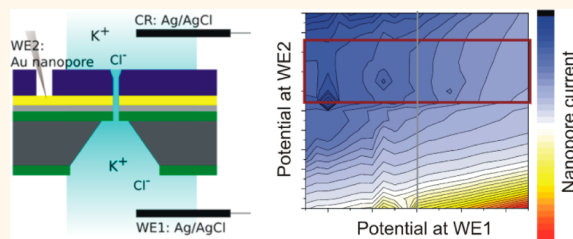


Mapping the Ion Current Distribution in Nanopore/Electrode Devices

Agnieszka Rutkowska, Joshua B. Edel, and Tim Albrecht*

Department of Chemistry, Imperial College London, Exhibition Road, South Kensington Campus, London SW7 2AZ, U.K.

ABSTRACT Solid-state nanopores with integrated electrodes have interesting prospects in next-generation single-molecule biosensing and sequencing. These include “gated” nanopores with a single electrode integrated into the membrane, as well as two-electrode designs, such as a transversal tunneling junction. Here we report the first comprehensive analysis of current flow in a three-electrode device as a model for this class of sensors. As a new feature, we observe apparent rectification in the pore current that is rooted in the current distribution of the cell, rather than the geometry or electrostatics of the pore. We benchmark our results against a recently developed theoretical model and define operational parameters for nanopore/electrode structures. Our findings thus facilitate the rational design of such sensor devices.



KEYWORDS: metallic nanopores · charge transfer resistance · ionic current rectification · multielectrode arrangement · electrode cross-coupling

Solid-state nanopores are versatile sensing platforms with applications in medicine and biochemistry.^{1,2} They allow for reliable, label-free, and high-throughput detection of charged biomolecules such as DNA, RNA, and proteins, at the single-molecule level. A conventional sensor device consists of a thin, free-standing dielectric membrane, which separates a liquid cell into two reservoirs with one electrode in each compartment, Figure 1A. A nanometer-scale pore (“nanopore”) in the membrane constitutes the only connection between the two reservoirs that allows ion, liquid, and analyte transport. Upon application of an external electric field, charged biomolecules in solution may be driven through the pore, depending on their charge, the magnitude of the electric field, and the properties of the pore.^{3,4} Each translocation event modulates the ion current through the system, providing information on molecular size, composition, and intermolecular interactions of the analyte.

Control of the translocation process is a significant challenge, but particularly important for high-precision measurements, *e.g.*, in DNA/RNA sequencing or molecular barcoding.⁵ In biological pores, incorporation of motor enzymes at the entrance of the pore using site-directed mutagenesis

has shown great promise;^{6–8} unfortunately, this option is not available for solid-state nanopore sensors. With regard to the latter, several avenues have been explored, including chemical surface modification to incorporate receptor groups^{9,10} and the integration of a gate electrode into the membrane,^{11–16} in order to control the local electrostatics. Since the local electric field at the nanopore is to a significant extent current-induced, affecting the current distribution in the liquid cell is another way of controlling the speed and direction of the translocation process.^{13,16,17} This is particularly relevant to nanopore/electrode structures as a new class of single-molecule biosensors, which may contain three, four, or more electrodes per device, each of which in principle representing an independent current source. Recent work in this area includes nanopore-based DNA transistors,^{14,18–20} capacitors,²¹ tunneling junctions,^{22,23} and rectification in chemically modified nanopores.^{24–31}

In particular, Stein *et al.* showed that ionic current rectification can be achieved by charge redistribution in a nanochannel³² which featured an additional metallic gate electrode inside the nanopore. This electrode was carefully isolated from the electrolyte with a thin insulating oxide layer, thus minimizing interfacial charge transfer

* Address correspondence to t.albrecht@imperial.ac.uk.

Received for review October 10, 2012 and accepted December 12, 2012.

Published online December 12, 2012
10.1021/nn304695y

© 2012 American Chemical Society

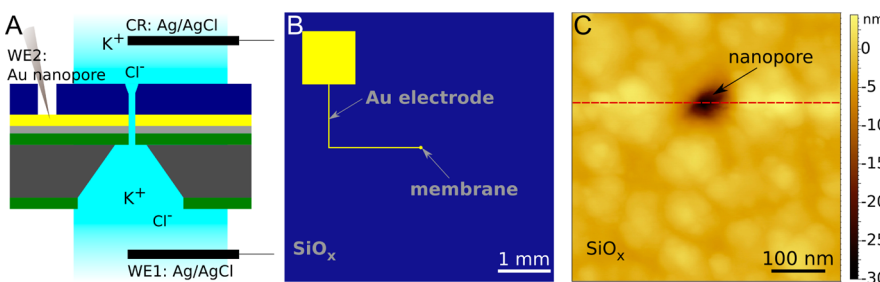


Figure 1. (a) Schematic of the electrochemical three-electrode setup with the nanopore device consisting of the following layers (not to scale): 30 nm Si_3N_4 (green), 5 nm Ti (light gray), 30 nm Au (yellow), and 150 nm SiO_x (dark blue) on a 300 μm silicon (dark gray). (b) Top view of the device structure showing the gold electrode geometry, including contact pad. The entire area of the device (5 mm \times 5 mm) is covered with SiO_x . (c) 1 μm \times 1 μm AFM tapping mode image of a nanopore milled through the top side of the device as shown in (a). The AFM image was deconvoluted using the Agilent imaging software for tip radii equal to 2 nm. The outer diameter of the pore was determined as 100 nm from the height profile, which is in-line with SEM imaging data (not shown).

reactions as much as possible (high charge transfer resistance, R_{ct}). In accordance with an electrostatic gating model, the transistor response was further shown to strongly depend on the solution pH and ionic strength.

However, charge transfer through any additional electrodes is not necessarily negligible, and R_{ct} may vary from very large to very small values, depending on the electrode potential, material, area, and solution conditions. Current understanding of its effect on the current distribution in a nanopore sensor and thus on the latter's performance is however very limited, especially when R_{ct} is not very large. To this end, one of us has recently proposed a basic theoretical model in an attempt to establish "safe" working conditions for a multielectrode nanopore sensor in different limits of R_{ct} and for different types of potential modulation.³³ On the basis of these results, it was found that the pore current and thus the apparent pore conductance are generally dependent on R_{ct} .

Here, we investigate this aspect in detail, both experimentally and from a theoretical point of view. In particular, we focus our attention on understanding the influence of Faradaic processes at the metallic membrane electrode on the nanopore current in terms of changes in R_{ct} . As a model system, we used a nanopore sensor in a bipotentiostatic setup (see the Experimental Section for details) with three electrodes, namely, two Ag/AgCl electrodes acting as working electrode 1 (WE1) and combined counter and reference electrode (CR), respectively, and a third, gold electrode (WE2), which is integrated into the membrane and whose charge transfer properties may be controlled by an applied potential. All potentials E_1 (for WE1) and E_2 (WE2) are quoted with respect to CR.

If no charge is transferred across the WE2/solution interface, the steady-state current I_2 at WE2 at constant E_1 and E_2 is zero. Then $R_{\text{ct}} \rightarrow \infty$, the interface is "perfectly polarizable", and E_2 has no effect on the magnitude of the transmembrane ionic current I_1 at WE1 beyond surface charge effects. In the opposite

limit, when interfacial charge transfer is facile, I_2 is high, and $R_{\text{ct}} \rightarrow 0$, the interface is "perfectly nonpolarizable".³⁴ In such a case, I_1 depends linearly on both potentials E_1 and E_2 . Notably, large enough E_2 can even cause inversion of I_1 . The embedded Au electrode WE2 in our nanopore devices may satisfy the entire R_{ct} range, depending on the conditions applied.

RESULTS AND DISCUSSION

The final device design used throughout the measurements is depicted in Figure 1A, including a schematic of the electrode setup and the liquid cell. A 1 M KCl aqueous solution was used as the electrolyte. The nanopore devices were fabricated using standard nanofabrication procedures, *cf.* Experimental Section for details.³⁵

The top view of the device geometry is shown in Figure 1B. The gold electrode consists of a square contact pad (1 mm \times 1 mm) and a micrometer-scale Au contact leading up to an Au disc, aligned to the nanopore membrane (free-standing area: 50 μm \times 50 μm). The Au electrode is covered with a silicon dioxide layer (thickness: 150 nm) as the insulating layer. Nanopores with a top diameter of 50–100 nm were milled using 5 s milling time and 1 pA beam current from the top side of the device (*i.e.*, through silicon dioxide as the first layer).

Figure 1C shows a representative high-resolution atomic force microscopy (AFM) topography image of a solid-state nanopore scanned from the silicon dioxide side using acoustic alternating contact mode. The imaging was performed using supersharp silicon tips, with radii of \sim 2 nm. The outer diameter of the nanopore is approximately 100 nm, consistent with SEM studies (data not shown). Similar results have been obtained for all nanopores fabricated using the same milling conditions (over 70 samples). The depth profile further indicates a gradual decrease in the nanopore internal diameter down to approximately 15 nm within the first 30 nm of the nanopore opening. These results are in line with previous studies, where the nanopore

opening was surrounded by a circular etched area much larger than the nanopore internal diameter.³⁶ A complex nanopore geometry may also be expected based on the layered membrane design and the different milling properties of the materials involved. For example, the milling rate of silicon dioxide is over five times slower than Au.³⁷ Further studies using transmission electron tomography are currently on the way to resolve the full three-dimensional topography of these layered nanopore structures.

The nanopore diameter was further examined by measuring conductance through nanopores in the standard two-electrode arrangement.^{4,34,38} We tested 20 devices and all gave similar $I_1 - E_1$ characteristics as described below. Each sample was cleaned by immersion in acetone for 30 min, followed by 75% and 50% (v/v) ethanol aqueous solutions and ultrapure (18.2 MΩ) water. Both sides of the device were exposed to oxygen plasma for 5 min each to remove any organic contaminants. Finally, the samples were immersed in 50% ethanol to facilitate surface wetting until the devices were used in further experiments.³⁹

The initial test experiments were conducted with WE2 disconnected from the electronic circuit. In this case, WE2 cannot sustain a steady-state (Faradaic) current, unless electrochemical reactions are induced by the transmembrane voltage between WE1 and CR, *e.g.*, as in "bipolar" electrochemistry.^{33,40} Figure S2 in the Supporting Information shows a typical current trace with I_1 being linearly dependent on E_1 and some degree of capacitive charging. From the slope, we obtained a conductance (resistance) of 2.3 nS (0.4 GΩ). Assuming an hourglass-shaped geometry, which is typical of nanopores drilled by FIB,³⁸ the internal diameter of the nanopore may be estimated to about 15 nm, *cf.* Supporting Information for further details on the calculations and underlying assumptions.

Once WE2 is connected and thus may act as a current source, the current distribution in the cell changes significantly. The $I_1(E_1)$ trace becomes non-Ohmic and depends strongly on E_2 .

Figure 2A and B plot the currents I_1 and I_2 , measured at the two working electrodes as a function of both potentials E_1 and E_2 . Both currents are recorded at steady state and thus do not contain any contributions from capacitive charging or transient redox processes on the electrode surfaces. The color scale in both graphs shows the range of the ionic current at the respective electrodes from highly negative (black and dark blue) to highly positive (dark red) values. The electroactive area of the gold membrane microelectrode appears to be larger than the area exposed inside the nanopore, which is likely due to pin holes in the SiO_x layer. This does not affect the functionality of the device in the sense of our study, but only decreases R_{ct} quantitatively. The Supporting Information contains a more detailed discussion of this aspect, including

further control experiments to establish the electroactive area of the membrane electrode.

Interestingly, over almost the entire range of E_1 and E_2 , I_1 and I_2 are similar in magnitude, but opposite in sign. Thus, the majority of the current in the cell flows between WE1 and WE2; the current at the CR, I_{CR} , is always small in comparison (calculated from Kirchoff's law: $\sum_{i=1}^n I_i = 0$; see Figure S3 in the Supporting Information). This is in accordance with its function as a (quasi) reference electrode inside the cell.⁴¹

I_1 increases from approximately -15 nA to 100 nA, as a function of both E_1 and E_2 . In the region of negative E_2 , I_1 increases linearly in the entire range of E_1 . On the other hand, there are two regimes in the region of positive E_2 . In the first one, for $E_2 \geq 0.7$ V, I_1 shows a similar, close to linear, trend to that for negative E_2 : the current decreases with more positive E_2 . However, for 0.1 V < E_2 < 0.7 V, the current is less dependent on E_2 . The green rectangle in Figure 2 indicates the relevant current range; see below and Figure 3 for a more detailed discussion of the cross-correlation between I_1 and I_2 . It is illustrative to follow the change in I_1 for the entire range of E_2 , say at $E_1 = 0$ V (gray line in Figure 2A): In this region I_1 increases steadily from approximately -1 nA for very positive E_2 to about 0.1 nA at $E_2 = 0$ V. In the negative range, I_1 increases more steeply with negative E_2 , reaching values of approximately 40 nA at $E_2 = -1$ V.

An analogous analysis of the current change as a function of both E_1 and E_2 is observed for I_2 , Figure 2B. The contour plot shows a strong dependence of I_2 on both potentials, apart from the intermediate region for E_2 between 0.1 and 0.7 V, for which the change of I_2 with E_2 is less significant.

Figure 2C illustrates the strong correlation between I_1 and I_2 (slope ~ 1), except for 0.4 nA > I_2 > -0.1 nA shown in panel D. In the latter region of small I_2 , R_{ct} is large and the effect of WE2 on the current distribution in the cell negligible. It is this region that is highlighted with the (green) rectangle in panels A, B, E, and F: The contour lines in the current are widely spaced; thus there is little dependence of the current on applied potential. It is also the preferred operational regime for electrostatic gating of nanopore transport. While electrostatic effects are well known to affect the pore conductance,^{3,4,12,13,16,19,32,42} they are unlikely to account for all the effects observed here. Even though the inner pore diameter is on the order of 15 nm (see above), where surface charge effects can be important, in our case the ion concentration is high (Debye length < 1 nm) and the surface contribution not too large.³ Faradaic currents at WE2 can have different origins, in terms of the molecular redox species involved. For example, oxygen reduction processes take place at the gold electrode for $E_2 < -0.5$ V (vs Ag/AgCl) under solution conditions used here (cyclic voltammetry (CV) data, not shown).

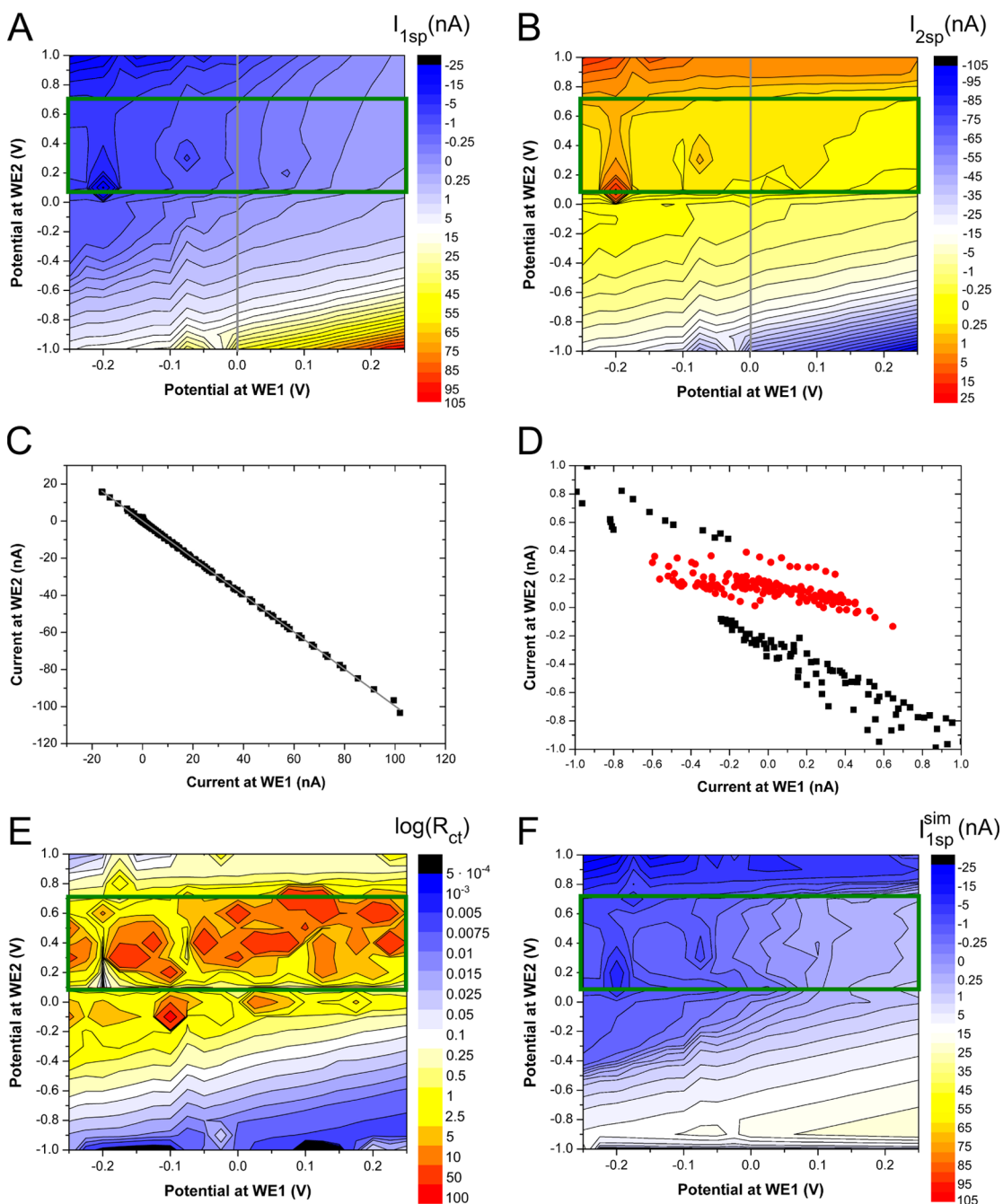


Figure 2. Simulation and experimental results for I_1 and I_2 at constant E_1 and E_2 , respectively. (A, B) Contour plots of the experimental steady-state currents I_1 and I_2 . The ion currents were measured in potential step experiments, where E_1 was stepped from 0 V to a potential in the range from -0.25 to $+0.25$ V at a constant E_2 ; currents were taken after 10 s in each step. (C) Cross correlation between I_1 and I_2 in the entire current range measured, and (D) in the range from -1 to $+1$ nA, at constant values of E_1 and E_2 . This demonstrates the strong correlation between the two currents, except when I_2 is small (and R_{ct} large). The red points in D correspond to the I_1 range independent of I_2 , which was in turn used to define the green rectangle in panels A, B, E, and F. (E) Experimentally determined values of R_{ct} based on data in B and eq 3, $\log(R_{\text{ct}})$ vs E_1 , E_2 plot. (F) Simulated I_1 as a function of E_1 and E_2 , based on eqs 1 and 1a, using experimental values of R_{ct} and two-dimensional least-squares fit values for R_{s2} and R_{pore} . See text for further details. The color scales in A, B, E, and F are as indicated; the black contour lines represent constant values of either ion current or $\log(R_{\text{ct}})$. The electrolyte was 1 M KCl.

Accordingly, the ionic current signal at the WE2 in this potential range ($I_2 < -10$ nA in Figure 2B) is negative. At sufficiently high E_2 , I_2 is positive due to oxidation reactions at WE2, e.g., water oxidation. In the intermediate region, where no Faradaic processes take place, the steady-state current is zero. Conversion of

Cl^- and AgCl at CR and WE1 is generally fast across the entire voltage range; hence the current–voltage relation is ohmic.

In order to elucidate the role of R_{ct} in more detail, we employed the above experimental data in conjunction with a recently proposed impedance model for current

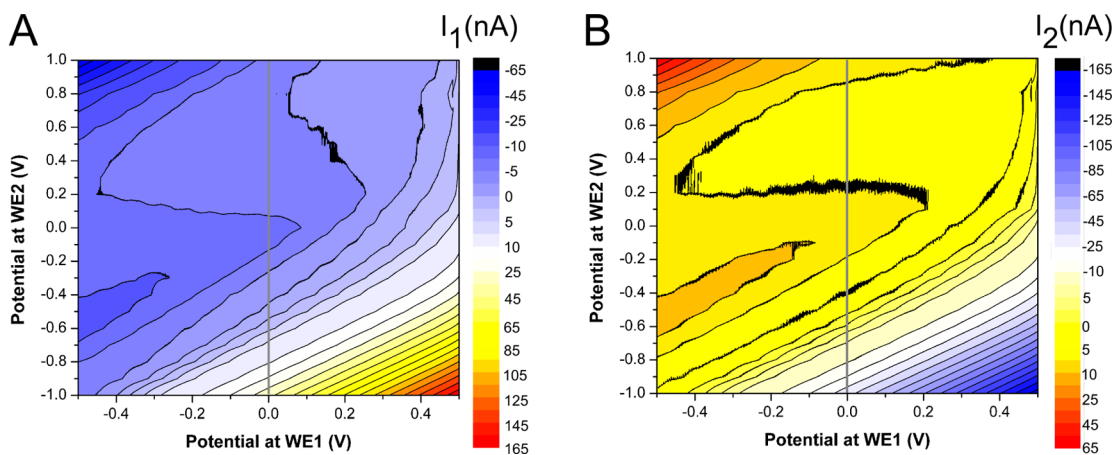


Figure 3. Contour plots of the transmembrane ionic current, I_1 (A), and of I_2 (B), as a function of both E_1 and E_2 in 1 M KCl aqueous solution. The colors correspond to the current range as shown in the current scale for WE1 and WE2, respectively, while the black contour lines represent a constant current value. E_1 was ramped from 0 to -0.5 V and $+0.5$ V and back to 0 V at a scan rate of 100 mV/s. E_2 was kept constant during each sweep. The gray lines in both contour plots are for reference.

flow in nanopore/electrode structures,³³ now extended to include explicit solution resistances in the respective compartments. Section 5 in the Supporting Information shows the equivalent circuit, parameter definitions, and further details on the derivation of eqs 1a and 2a.

Solving the impedance model for the currents at WE1 and WE2, I_1 and I_2 , allows for a direct comparison between experimental data and simulated results. For the steady-state currents, this yields (constant E_1 and E_2 , neglecting transient currents)

$$I_1 = \frac{R_{s2'} + R_{ct} + R_{s2}}{A} E_1 - \frac{R_{s2}}{A} E_2 \quad (1)$$

$$A = R_{pore} R_{s2'} + R_{s1} R_{ct} + R_{s2''} R_{ct} + R_{s1} R_{s2'} + R_{s2} R_{ct} + R_{pore} R_{ct} + R_{s2} R_{pore} + R_{s2} R_{s2''} + R_{s2} R_{s1} + R_{s2} R_{s2''} + R_{s2''} R_{s2'} \quad (1a)$$

$$I_2 = \frac{R_{s2}}{B} E_1 + \frac{R_{s1} + R_{s2} + R_{s2''} + R_{pore}}{B} E_2 \quad (2)$$

$$B = (R_{s2} + R_{pore} + R_{s1} + R_{s2''}) R_{ct} + R_{s1} R_{s2'} + R_{s2} R_{pore} + R_{s2} R_{s2''} + R_{s2} R_{s1} + R_{pore} R_{s2''} + R_{s2} R_{s1} + R_{s2''} R_{s2'} \quad (2a)$$

The current through CR, I_{CR} , may again be calculated from Kirchhoff's law knowing I_1 and I_2 ; see above. Interestingly, based on this model, the different contributions to solution resistance are not equivalent, in terms of their effect on the pore current I_1 . The magnitude of R_{s2} in particular will determine the potential drop across the nanopore and thus the value of I_1 . R_{s1} , $R_{s2'}$, and $R_{s2''}$ have a negligible effect in this context, as long as R_{pore} is sufficiently large. For simulation purposes, we will assume 100 Ω for all solution resistances, except R_{s2} ; see below. The order of magnitude is comparable to values obtained in conventional electrochemical experiments, and since their effect is small, the associated error is negligible. In principle,

R_{pore} and R_{ct} are accessible experimentally, the former through the two-electrode conductance measurements reported above ($R_{pore} \approx 0.4$ G Ω), the latter through data shown in Figure 2B.

To this end, we use the definition of R_{ct} at steady state and constant potentials E_1 and E_2 :

$$R_{ct}^{-1} = \left(\frac{dI_2}{dE_2} \right)_{E_1 \text{CR}} \quad (3)$$

to calculate R_{ct} for all combinations of E_1 and E_2 . The result is shown in Figure 2E, as $\log(R_{ct})$ vs E_1 , E_2 plot.

The changes in R_{ct} are clearly visible in the entire range of both potentials from low resistance values (black and dark blue regions of $\log R_{ct} < 0.1$ for $E_1 \leq -0.5$ V and $E_1 \geq 0.9$) to high R_{ct} (orange and red regions of $\log R_{ct} > 2.5$ for $0.1 \leq E_1 \leq 0.7$ V). As noted above, areas with large R_{ct} values correspond to potential regions where E_2 has little effect on I_1 . Low R_{ct} values imply relatively large currents at WE2 and therefore a strong effect on I_1 .

We now take these experimental R_{ct} values to calculate the nanopore current I_1 , based on eqs 1–2a. However, for $R_{pore} = 0.4$ G Ω and $R_{s2} = 100 \Omega$, the correspondence between experimental and simulated data was rather poor (not shown). In particular, the variation of I_1 with E_2 came out too small in the simulations, which clearly indicates a shortcoming in the underlying model. We then performed a two-dimensional least-squares of the simulated I_1 values to the experimental ones, with R_{s2} and R_{pore} as fitting parameters. The fit converged for $R_{pore} = 42.5$ M Ω and $R_{s2} = 368$ M Ω ; the resulting error surface around the best fit is shown in Figure S5 (the parameter space was explored more widely). These values are significantly different from the experimentally obtained R_{pore} and any reasonable estimate for R_{s2} . Upon inspection of eq 1, however, it becomes clear that the large value for R_{s2} simply accounts for the experimentally observed

strong dependence of I_1 on E_2 . The latter is likely due to cross-coupling between the two electrodes, for example when current flow at WE1 affects the potential drop at the WE2/solution interface, and thus the current at WE2. This effect is not included in the model, hence the relatively poor numerical agreement.

However, while not entirely adequate in quantitative terms, the simulation does capture the experimentally observed trends qualitatively over the wide range of E_1 and E_2 studied (using the fitted values for R_{pore} and R_{s2}), Figure 2F (to be compared with Figure 2A). Specifically, in the region of large R_{ct} (green rectangle, *cf.* Figure 2E, the contour lines are approximately parallel to the (vertical) E_2 axis, indicating that the pore current I_1 does not change significantly with E_2 in this region. On the other hand, I_1 does change with E_1 , from approximately -5 to $+5$ nA for $-0.25 \text{ V} < E_1 < +0.25 \text{ V}$ in Figure 2A (experimental data) and from approximately -1 to $+1$ nA in the same potential region in Figure 2F (simulations). When R_{ct} is smaller and more current is passing through the membrane electrode, I_1 is dependent on both E_1 and E_2 . In Figure 2A and F, this corresponds to regions where the contour lines are diagonal. This is seen both experimentally and in the simulations for large values of E_1 and E_2 , in line with our argument that the corresponding currents are driven by Faradaic processes. The denser the contour lines, the stronger the variation of I_1 with E_1 and E_2 , respectively. As noted previously, capacitive charging does not play a role under these circumstances, since the currents were recorded under steady-state conditions. As for the high- R_{ct} region, the simulated current variation remains smaller than in the experiment, despite using the fitted values for R_{pore} and R_{s2} . Thus, the model does account for the overall behavior of the sensor device, based on variations in R_{ct} . Further refinement is needed to achieve greater quantitative precision, which is perhaps to be expected, given the simplicity of the initial model. One effect that is not part of the current model is the formation of parallel current paths across the membrane, in effect bypassing R_{pore} and increasing the current measured at I_1 . Cracks in the membrane can have such an effect in principle. However, in the present case we believe the physical origin to be more subtle. As mentioned above, I_1 is in agreement with the pore conductance predicted from the pore dimensions, if the membrane electrode is disconnected from the electric circuit. This means that the membrane itself is intact. On the other hand, the Si core of the chip is conductive and could constitute an additional current path, provided it is electrically coupled to the liquid on both sides of the membrane. On the basis of the chip design shown in Figure 1, it is not clear what the nature of this (putative) current path could be, but it would to some extent explain why the experimental values of I_1 are higher than expected based on our model. Importantly, if E_1 also affects the

potential drops at the membrane/solution interfaces, changes in E_1 would also result in a modulation of this additional current path, due to changes in the Faradaic coupling to the solution. Such effects are not part of our current model, leading to an underestimation of the simulated current, compared to the experimental value. Their incorporation in a standard impedance model may not be trivial, due to the cross-coupling between the different potentials and currents, and is beyond the scope of the present work. Again, capacitive effects do not play a role, as long as steady-state currents are measured.

Accordingly, we also investigated the characteristics of the nanopore sensor, when E_1 is ramped linearly with time, at constant E_2 (CV). This configuration is often used for nanopore characterization, *e.g.*, to determine the pore conductance or investigate rectification effects. It is however unclear whether the presence of WE2 allows for a direct connection between measured conductance and pore dimensions to be made. Our basic model predicts that the slope of the $I_1(E_1)$ trace still gives $1/R_{\text{pore}}$, irrespective of R_{ct} , as long as $R_{\text{pore}} \gg R_{\text{s2}}$. On the contrary, the steady-state current I_1 at constant E_1 , E_2 does depend on R_{ct} and is no longer related to pore dimensions in a simple manner. Apart from capacitive charging of the membrane/chip device, additional effects that are not part of the model may affect the current distribution in the cell, such as transient surface-confined redox processes and potentially space-charge effects close to the nanopore opening.

Figure 3A, B shows the contour plots of the ionic current as a function of both E_1 and E_2 , when cycling E_1 between -0.5 and $+0.5 \text{ V}$ (starting at 0 V ; currents reported are from the positive scanning direction) with a scan rate 100 mV/s at constant E_2 ; I_1 and I_2 were monitored simultaneously. Notably, the magnitude of both currents I_1 and I_2 is larger by up to 40 nA for the largest potential differences ($E_1 = \pm 0.5 \text{ V}$ and $E_2 = \pm 1.0 \text{ V}$), compared to the corresponding ion current at steady state (Figure 2A, B). The increase in ion current is due to capacitive charging, which contributes to the signal along with the Faradaic current. Again, we observe a strong correlation between I_1 and I_2 and even current reversal, *e.g.*, in I_1 for small (positive) E_1 , but large (negative) E_2 . Accordingly, apparent strong rectification effects arise in I_1 , depending on E_2 . As noted above, however, these are not rooted in the charge distribution in the nanopore, but due to charge transfer effects at WE2. This is also why both sets of $I(E)$ data become nonlinear at the extreme values of E_2 (more narrowly spaced contour lines), where redox processes are more pronounced (oxidation at large positive E_2 , reduction at large negative E_2).

Figure 4 illustrates the effect of the charge transfer properties of WE2 on the nanopore conductance G_{pore} (at $E_1 = 0 \text{ V}$); the charge transfer conductance

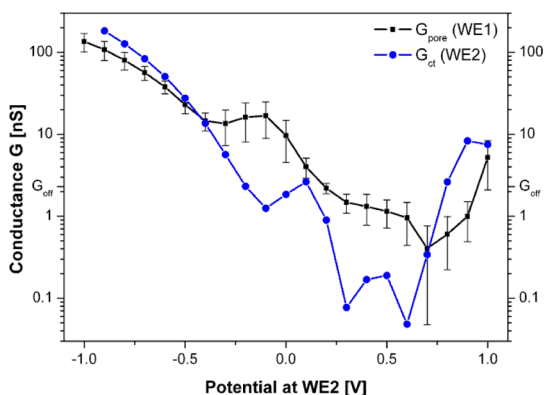


Figure 4. Nanopore conductance G_{pore} (squares, black curve) and charge transfer conductance $G_{\text{ct}} = R_{\text{ct}}^{-1}$ (circles, blue curve) as a function of E_2 . G_{pore} was determined from $I_1(E_1)$ traces in the range of $E_1 = \pm 50$ mV at constant E_2 ; G_{ct} from current measurements at constant potentials E_1 and E_2 , according to eq 3 and Figure 2. G_{off} indicates the nanopore conductance measured in an $I_1(E_1)$ scan with WE2 disconnected (2.3 nS).

$G_{\text{ct}} = R_{\text{ct}}^{-1}$ is plotted for convenience. Note that G_{ct} was recorded at WE2 under steady-state conditions and thus does not contain any contributions from capacitive charging. G_{off} is the pore conductance measured with WE2 disconnected; see Figure S2 in the Supporting Information ($G_{\text{off}} = 2.3$ nS). Generally, G_{pore} follows G_{ct} ; that is, the measured sensing signal I_1 depends markedly on the charge transport properties of the WE2/solution interface (mass transport, surface reactivity, and area). However, in accordance with our theoretical model, this is no longer the case once G_{ct} is significantly lower than G_{off} . Then $G_{\text{pore}} \approx G_{\text{off}}$ (within experimental error), and I_1 is no longer affected by WE2, except for local surface charge effects. Interestingly, the behavior for $-0.4 \text{ V} < E_2 < 0 \text{ V}$ seems to depart from the direct proportionality between G_{ct} and G_{pore} in that G_{pore} increases (slightly) with decreasing G_{ct} . It is possible that this effect is due to charging of the gold

surface inside the pore, before charge transfer effects become dominant again at larger potentials E_2 . Its magnitude is small though, as expected for a surface effect under the given conditions, and close to experimental error. Note that the potential of zero charge for Au is on the order of 0.3 V vs Ag/AgCl, depending on the crystallinity of the surface, where the measured G_{pore} in Figure 4 is indeed lowest.⁴³

CONCLUSION

In summary, we have studied the ion current distribution in a three-electrode nanopore sensor as a model system for multielectrode nanopore devices. While previous studies have focused on electrostatic gating inside the nanopore by means of a well-insulated gate electrode embedded into the membrane ($R_{\text{ct}} \rightarrow 0$), for the first time we combine experimental and modeling data to develop a comprehensive understanding of sensor performance for the whole range of R_{ct} , *i.e.*, from very large to very small values. Electrochemical charge transfer processes at the WE2 caused significant changes in the nanopore device characteristics, affecting the local electric field at the nanopore and resulting in pronounced ionic current rectification at high salt concentrations. A simple three-electrode impedance model was shown to predict the qualitative features of current flow in such a system, but further refinement is needed to achieve better quantitative agreement. Our results thus make an important contribution to the rational design of nanopore sensors with integrated electrodes with three and more current sources, such as in nanopore-based tunneling junctions for biopolymer sequencing. Finally, a detailed understanding of how such additional electrodes affect the current distribution in the cell may offer new ways to control the translocation process itself, which is still one of the major challenges in nanopore sensing on the way to a routine high-resolution and high-fidelity biosensing tool.

EXPERIMENTAL SECTION

Device Fabrication. The device microfabrication protocol is illustrated in Figure S1 in the Supporting Information. Briefly, both sides of a 300 μm (100) silicon wafer were coated with a 30 nm silicon nitride layer using low-pressure chemical vapor deposition. Reactive ion etching was used to partially etch the silicon nitride film on one side of the wafer (bottom side). Thirty-nanometer gold microelectrodes (with 5 nm titanium adhesive layer) were deposited on the top side using conventional photolithography and electron beam sputtering techniques, followed by photoresist lift-off. The final Ti/Au film thickness was measured using acoustic alternating contact atomic force microscopy. Anisotropic KOH wet etching of silicon resulted in the formation of a 50 μm free-standing Au/Ti/Si_xN_y membrane. Finally, a *ca.* 150 nm thick silicon dioxide film was deposited onto the device's top side using plasma-enhanced CVD (PE-CVD).

Prior to SiO_x PE-CVD, the wafer was cleaned by immersion in acetone for 30 min, followed by 75% and 50% ethanol aqueous solutions and water. Finally, it was exposed to oxygen plasma

for 10 min each side. PE-CVD resulted in SiO_x film with a thickness of 152 ± 7 nm and surface roughness below 6 nm as measured using ellipsometry and AFM, respectively.

Nanopore fabrication was performed using dual beam focused ion beam/scanning electron microscopy (SEM), as described previously.³⁵

AFM Imaging. AFM imaging of solid-state nanopores was carried out using the ACC mode of an Agilent Technologies 550 scanning probe microscope and super sharp silicon probes (SSS-NCH-20, Nanosensors).

Electrochemical Cell Setup. All electrochemical measurements were performed in a polyether ether ketone cell fabricated in-house, consisting of two reservoirs (*cis* and *trans*) filled with 1 M KCl aqueous solution. The compartments were separated with a nanopore device as shown in Figure 1a, with the silicon dioxide layer facing up (Figure S1). The 1 mm \times 1 mm gold square pad (Figure 1b) was isolated from the solution. Kwik-cast epoxy (World Precision Instruments) was used to keep the sample in place and to ensure no leakage between the two compartments. A 5 μm tungsten probe was used to create an

electrical contact between the metallic nanopore and the external electronic circuit, by micropositioning the needle onto the gold square pad and scratching the SiO_x layer locally over the gold film.

Silver wires with silver chloride coating were prepared in-house and used as quasi-counter and reference electrode and first working electrode in the top (*cis*) and bottom (*trans*) reservoirs, respectively. The metallic nanopore acted as the second WE.

All measurements were performed using a bipotentiostatic setup (CH Instruments, CHI760C).

Data Processing. All contour plots were generated using Origin software (OriginPro 8.5.0 SRI) by creating a matrix of current or charge transfer resistance values for given E_1 and E_2 ranges using the Renka–Cline method.

Conflict of Interest: The authors declare no competing financial interest.

Supporting Information Available: Figures showing (i) nanopore device microfabrication, (ii) electrochemical cell setup, (iii) nanopore conductance in the hourglass model, (iv) ionic current at the counter/reference electrode, (v) electric equivalent circuit of the three-electrode setup, (vi) verification of the theoretical model of ionic current distribution in the cell, (vii) simulated contour plots of $I_1(E_1, E_2)$, when E_1 is ramped at constant E_2 . This material is available free of charge via the Internet at <http://pubs.acs.org>.

Acknowledgment. This work was supported in part by a European Research Council Starting Investigator grant (J.B.E.) and a Leverhulme Trust research grant (A.R.).

REFERENCES AND NOTES

1. Dekker, C. Solid-State Nanopores. *Nat. Nanotechnol.* **2007**, *2*, 209–215.
2. Venkatesan, B. M.; Bashir, R. Nanopore Sensors for Nucleic Acid Analysis. *Nat. Nanotechnol.* **2011**, *6*, 615–624.
3. Ayub, M.; Ivanov, A.; Instuli, E.; Cecchini, M.; Chansin, G.; McGilvery, C.; Hong, J. G.; Baldwin, G.; McComb, D.; Edel, J. B.; *et al.* Nanopore/Electrode Structures for Single-Molecule Biosensing. *Electrochim. Acta* **2010**, *55*, 8237–8243.
4. Smeets, R. M. M.; Keyser, U. F.; Krapf, D.; Wu, M. Y.; Dekker, N. H.; Dekker, C. Salt Dependence of Ion Transport and DNA Translocation through Solid-State Nanopores. *Nano Lett.* **2006**, *6*, 89–95.
5. Wanunu, M. Nanopores: A Journey towards DNA Sequencing. *Phys. Life Rev.* **2012**, *9*, 125–158.
6. Banerjee, A.; Mikhailova, E.; Cheley, S.; Gu, L. Q.; Montoya, M.; Nagaoka, Y.; Gouaux, E.; Bayley, H. Molecular Bases of Cyclodextrin Adapter Interactions with Engineered Protein Nanopores. *Proc. Natl. Acad. Sci. U. S. A.* **2010**, *107*, 8165–8170.
7. Rincon-Restrepo, M.; Mikhailova, E.; Bayley, H.; Maglia, G. Controlled Translocation of Individual DNA Molecules through Protein Nanopores with Engineered Molecular Brakes. *Nano Lett.* **2011**, *11*, 746–750.
8. Stoddart, D.; Heron, A. J.; Klingelhoefer, J.; Mikhailova, E.; Maglia, G.; Bayley, H. Nucleobase Recognition in ssDNA at the Central Constriction of the alpha-Hemolysin Pore. *Nano Lett.* **2010**, *10*, 3633–3637.
9. Wanunu, M.; Meller, A. Chemically Modified Solid-State Nanopores. *Nano Lett.* **2007**, *7*, 1580–1585.
10. Wei, R. S.; Gatterdam, V.; Wieneke, R.; Tampe, R.; Rant, U. Stochastic Sensing of Proteins with Receptor-Modified Solid-State Nanopores. *Nat. Nanotechnol.* **2012**, *7*, 257–263.
11. Ai, Y.; Liu, J.; Zhang, B. K.; Qian, S. Field Effect Regulation of DNA Translocation through a Nanopore. *Anal. Chem.* **2011**, *82*, 8217–8225.
12. He, Y. H.; Tsutsui, M.; Fan, C.; Taniguchi, M.; Kawai, T. Gate Manipulation of DNA Capture into Nanopores. *ACS Nano* **2011**, *5*, 8391–8397.
13. He, Y. H.; Tsutsui, M.; Fan, C.; Taniguchi, M.; Kawai, T. Controlling DNA Translocation through Gate Modulation of Nanopore Wall Surface Charges. *ACS Nano* **2011**, *5*, 5509–5518.
14. Jiang, Z. J.; Stein, D. Charge Regulation in Nanopore Ionic Field-Effect Transistors. *Phys. Rev. E* **2011**, *83*, 031203.
15. Yen, P. C.; Wang, C. H.; Hwang, G. J.; Chou, Y. C. Gate Effects on DNA Translocation through Silicon Dioxide Nanopore. *Rev. Sci. Instrum.* **2012**, *83*, 034301.
16. Karnik, R.; Fan, R.; Yue, M.; Li, D. Y.; Yang, P. D.; Majumdar, A. Electrostatic Control of Ions and Molecules in Nanofluidic Transistors. *Nano Lett.* **2005**, *5*, 943–948.
17. White, R. J.; White, H. S. Influence of Electrophoresis Waveforms in Determining Stochastic Nanoparticle Capture Rates and Detection Sensitivity. *Anal. Chem.* **2007**, *79*, 6334–6340.
18. Luan, B. Q.; Peng, H. B.; Polonsky, S.; Rossnagel, S.; Stolovitzky, G.; Martyna, G. Base-By-Base Ratcheting of Single Stranded DNA through a Solid-State Nanopore. *Phys. Rev. Lett.* **2010**, *104*, 238103.
19. Nam, S. W.; Rooks, M. J.; Kim, K. B.; Rossnagel, S. M. Ionic Field Effect Transistors with Sub-10 nm Multiple Nanopores. *Nano Lett.* **2009**, *9*, 2044–2048.
20. Polonsky, S.; Rossnagel, S.; Stolovitzky, G. Nanopore in Metal-Dielectric Sandwich for DNA Position Control. *Appl. Phys. Lett.* **2007**, *91*, 153103.
21. Gracheva, M. E.; Vidal, J.; Leburton, J. P. p-n Semiconductor Membrane for Electrically Tunable Ion Current Rectification and Filtering. *Nano Lett.* **2007**, *7*, 1717–1722.
22. Ohshiro, T.; Matsubara, K.; Tsutsui, M.; Furushashi, M.; Taniguchi, M.; Kawai, T. Single-Molecule Electrical Random Resequencing of DNA and RNA. *Sci. Rep.* **2012**, *2*, 501.
23. Tsutsui, M.; Rahong, S.; Izumi, Y.; Okazaki, T.; Taniguchi, M.; Kawai, T. Single-Molecule Sensing Electrode Embedded In-Plane Nanopore. *Sci. Rep.* **2011**, *1*, 46.
24. Siwy, Z. S.; Howorka, S. Engineered Voltage-Responsive Nanopores. *Chem. Soc. Rev.* **2010**, *39*, 1115–1132.
25. Constantin, D.; Siwy, Z. S. Poisson-Nernst-Planck Model of Ion Current Rectification through a Nanofluidic Diode. *Phys. Rev. E* **2007**, *76*, 041202.
26. He, Y.; Gillespie, D.; Boda, D.; Vlassiouk, I.; Eisenberg, R. S.; Siwy, Z. S. Tuning Transport Properties of Nanofluidic Devices with Local Charge Inversion. *J. Am. Chem. Soc.* **2009**, *131*, 5194–5202.
27. Kalman, E. B.; Sudre, O.; Vlassiouk, I.; Siwy, Z. S. Control of Ionic Transport through Gated Single Conical Nanopores. *Anal. Bioanal. Chem.* **2009**, *394*, 413–419.
28. Kalman, E. B.; Vlassiouk, I.; Siwy, Z. S. Nanofluidic Bipolar Transistors. *Adv. Mater.* **2008**, *20*, 293–297.
29. Nguyen, G.; Vlassiouk, I.; Siwy, Z. S. Comparison of Bipolar and Unipolar Ionic Diodes. *Nanotechnology* **2010**, *21*, 265301.
30. Siwy, Z. S. Ion-Current Rectification in Nanopores and Nanotubes with Broken Symmetry. *Adv. Funct. Mater.* **2006**, *16*, 735–746.
31. Vlassiouk, I.; Smirnov, S.; Siwy, Z. Nanofluidic Ionic Diodes. Comparison of Analytical and Numerical Solutions. *ACS Nano* **2008**, *2*, 1589–1602.
32. Stein, D.; Kruithof, M.; Dekker, C. Surface-Charge-Governed Ion Transport in Nanofluidic Channels. *Phys. Rev. Lett.* **2004**, *93*, 035901.
33. Albrecht, T. How to Understand and Interpret Current Flow in Nanopore/Electrode Devices. *ACS Nano* **2011**, *5*, 6714–6725.
34. Ayub, M.; Ivanov, A.; Hong, J.; Kuhn, P.; Instuli, E.; Edel, J. B.; Albrecht, T. Precise Electrochemical Fabrication of sub-20 nm Solid-State Nanopores for Single-Molecule Biosensing. *J. Phys.: Condens. Matter* **2010**, *22*, 454128.
35. Ivanov, A. P.; Instuli, E.; McGilvery, C. M.; Baldwin, G.; McComb, D. W.; Albrecht, T.; Edel, J. B. DNA Tunneling Detector Embedded in a Nanopore. *Nano Lett.* **2011**, *11*, 279–285.
36. Liebes, Y.; Hadad, B.; Ashkenasy, N. Effects of Electrons on the Shape of Nanopores Prepared by Focused Electron Beam Induced Etching. *Nanotechnology* **2011**, *22*, 285303.

37. Orloff, K.; Swanson, L.; Utlaut, M. W. *High Resolution Focused Ion Beams: FIB and its Applications*. Springer: Berlin, 2003.
38. Kowalczyk, S. W.; Grosberg, A. Y.; Rabin, Y.; Dekker, C. Modeling the Conductance and DNA Blockade of Solid-State Nanopores. *Nanotechnology* **2011**, *22*, 315101.
39. Smeets, R. M. M.; Keyser, U. F.; Dekker, N. H.; Dekker, C. Noise in Solid-State Nanopores. *Proc. Natl. Acad. Sci. U. S. A.* **2008**, *105*, 417–421.
40. Fleischmann, M.; Ghoroghchian, J.; Rolison, D.; Pons, S. Electrochemical Behaviour of Dispersions of Spherical Ultramicroelectrodes. *J. Phys. Chem.* **1986**, *90*, 6392–6400.
41. Bard, A. J.; Faulkner, L. R. *Electrochemical Methods: Fundamentals and Applications*, 2nd ed.; Wiley: New York, 2006.
42. Schoch, R. B.; Han, J. Y.; Renaud, P. Transport Phenomena in Nanofluidics. *Rev. Mod. Phys.* **2008**, *80*, 839–883.
43. Dakkuori, A. S.; Kolb, D. M. Reconstruction of Gold Surfaces. In *Interfacial Electrochemistry*; Wieckowsky, A., Ed.; Marcel Dekker Inc.: Amsterdam, 1999.